

This is an Open Access document downloaded from ORCA, Cardiff University's institutional repository:<https://orca.cardiff.ac.uk/id/eprint/115414/>

This is the author's version of a work that was submitted to / accepted for publication.

Citation for final published version:

Tian, Mingjiao, Ma, Mudi, Xu, Bitao, Chen, Changwei, He, Chi, Hao, Zhengping and Albilali, Reem 2018. Catalytic removal of 1,2-dichloroethane over LaSrMnCoO₆/H-ZSM-5 composite: insights into synergistic effect and pollutant-destruction mechanism. *Catalysis Science and Technology* 8 (17) , pp. 4503-4514. 10.1039/C8CY00950C

Publishers page: <http://dx.doi.org/10.1039/C8CY00950C>

Please note:

Changes made as a result of publishing processes such as copy-editing, formatting and page numbers may not be reflected in this version. For the definitive version of this publication, please refer to the published source. You are advised to consult the publisher's version if you wish to cite this paper.

This version is being made available in accordance with publisher policies. See <http://orca.cf.ac.uk/policies.html> for usage policies. Copyright and moral rights for publications made available in ORCA are retained by the copyright holders.



Catalytic removal of 1,2-dichloroethane over LaSrMnCoO₆/H-ZSM-5 composite: insights into synergistic effect and pollutant-destruction mechanism†

Mingjiao Tian,^a Mudi Ma,^a Bitao Xu,^a Changwei Chen,^a Chi He,^a Zhengping Hao^{ab} and Reem Albilali^c

La_xSr_{2-x}MnCoO₆ materials with different Sr contents were prepared by a coprecipitation method, with LaSrMnCoO₆ found to be the best catalyst for 1,2-dichloroethane (DCE) destruction (T₉₀ = 509 °C). As such, a series of LaSrMnCoO₆/H-ZSM-5 composite materials were rationally synthesized to further improve the catalytic activity of LaSrMnCoO₆. As expected, the introduction of H-ZSM-5 could remarkably enlarge the surface area, increase the number of Lewis acid sites, and enhance the mobility of the surface adsorbed oxygen species, which consequently improved the catalytic activity of LaSrMnCoO₆. Among all the composite materials, 10 wt% LaSrMnCoO₆/H-ZSM-5 possessed the highest catalytic activity, with 90% of 1,2-DCE destructed at 337 °C, which is a temperature reduction of more than 70 °C and 170 °C compared with that of H-ZSM-5 (T₉₀ = 411 °C) and LaSrMnCoO₆ (T₉₀ = 509 °C), respectively. Online product analysis revealed that CO₂, CO, HCl, and Cl₂ were the primary products in the oxidation of 1,2-DCE, while several unfavorable reaction by-products, such as vinyl chloride, 1,1,2-trichloroethane, trichloroethylene, perchloroethylene, and acetaldehyde, were also formed via dechlorination and dehydrochlorination processes. Based on the above results, the reaction path and mechanism of 1,2-DCE decomposition are proposed.

1. Introduction

Volatile organic compounds (VOCs), regarded as a class of important pollutants, have attracted significant attention from researchers. Among these, chlorinated volatile organic compounds (CVOCs) are especially considered as main contributors to air pollution owing to their high toxicity, excellent stability, and low biodegradability.^{1,2} Therefore, the effective elimination of CVOCs is of great significance for air pollution

control. Various control methods, such as absorption/adsorption,^{3,4} catalytic combustion,⁵ plasma,⁶ pyrolysis,⁷ and the catalytic chemical vapor deposition of VOCs,⁸ have been exploited to solve this problem, among which catalytic combustion is recognized as one of the most promising technologies for CVOC removal, ascribed to its low operating temperature, high activity and selectivity, and recoverable heat.⁹

To date, researchers have focused on a large number of materials for the catalytic combustion of CVOCs, including noble-metal-supported catalysts, transition-metal-oxide-based catalysts and molecular-sieve catalysts (H-zeolite).^{2,10,11} Noble-metal-supported catalysts possess satisfactory catalytic activity at low temperature, but their practical applications are greatly limited by their high cost, inferior thermal stability, and low resistance to poisoning, especially in the case of CVOCs destruction.¹² Transition-metal-oxide-based catalysts are considered to be the most favorable materials in the oxidation of CVOCs due to their high catalytic activity and excellent resistance to chlorine poisoning and coking.² González-Prior et al. revealed that Co-metal-based catalysts are one type of efficient materials in the oxidation of 1,2-dichloroethane, and they proposed that the high content of surface oxygen species and good mobility of oxygen species through the

^a Department of Environmental Science and Engineering, State Key Laboratory of Multiphase Flow in Power Engineering, School of Energy and Power Engineering, Xi'an Jiaotong University, Xi'an 710049, Shaanxi, P.R. China.

E-mail: chi_he@xjtu.edu.cn; Fax: +86 29 8266 3857; Tel: +86 29 8266 3857

^b Cardiff Catalysis Institute, School of Chemistry, Cardiff University, Main Building, Park Place, Cardiff, CF10 3AT, UK

^c National Engineering Laboratory for VOCs Pollution Control Material & Technology, University of Chinese Academy of Sciences, Beijing 101408, P.R. China

^d Department of Chemistry, College of Science, Imam Abdulrahman Bin Faisal University, P.O. Box 1982, Dammam 31441, Saudi Arabia

† Electronic supplementary information (ESI) available: XRD, physicochemical properties and catalytic performance of La_xSr_{2-x}MnCoO₆ materials. By-products distribution of 0.1LSMC/Z sample. See DOI: 10.1039/c8cy00950c

lattice are the main advantages of cobalt metal oxides for CVOC combustion.¹³ Yang et al. reported that the efficient trichloroethylene catalytic activity of cerium–transition metal mixed oxide (4Ce1M, M = V, Cr, Mn, Fe, Co, Ni, and Cu) catalysts could be ascribed to their large specific surface areas and the strong interaction between CeO₂ and the transition metal oxides.¹⁴ However, the low surface area of metal oxides could limit their catalytic performance in oxidation processes. H-zeolites (such as H-ZSM-5) were also reported as a kind of efficient material in the oxidation of CVOCs, while H-zeolites with abundant acid sites suffer from deactivation caused by coking and chlorinated species attack during the CVOC destruction processes.¹⁵ Therefore, it is of great importance to design materials that combine the advantages of transition metal oxides and H-zeolites for the highly-efficient destruction of CVOCs.

Perovskite-type oxides (ABO₃), as one kind of common transition metal mixed oxides, have been intensively investigated in the field of VOCs oxidation owing to their good redox ability and availability.¹⁶ The A site (lanthanide, alkaline, or alkaline-earth cation) and B site (transition metals) in ABO₃ are able to coordinate the structure and control the reduction/oxidation property of perovskite-type oxides, respectively.¹⁷ In most cases, the A site cation in perovskite-type oxides for VOC oxidation is the lanthanum element (La). It is reported that the partial substitution of the A site cation by Sr atoms can significantly influence the physicochemical property of perovskite materials and consequently modulate their catalytic activity.¹⁸ Simultaneously, appropriate B site cations are also of great importance to improve the catalytic activity of perovskite-type oxides in the destruction of VOCs. Among these, La_{1-x}Sr_xMO₃ (M = Co, Mn) oxides have been proved to be the materials with the best catalytic performance for methane and CO oxidation.¹⁹ LaMnO₃ was proved to exhibit superior catalytic activity in the oxidation of vinyl chloride below 550 °C.²⁰ Zhang et al. reported that LaMnO_x catalysts exhibited good catalytic activity and high stability in the oxidation of 1,2-dichloropropane.²

In recent years, double-perovskite-type oxides (AA'BB'O₆, A₂BB'O₆, or AA'B₂O₆) with more expansive combination spaces between the different matching of A/A' and B/B' metals and higher chlorine resistance and structural stability than those of perovskite-type oxides have attracted extensive attention in the fields of solid-state electronics, fuel cells, and heterogeneous catalysis.^{21–23} However, the utilization of double-perovskite-type oxides in the catalytic oxidation of CVOCs has not been reported in the literature up to now, which leaves a large portion of the field to investigate and to provide valuable and new insights for the design and optimization of catalysts for the destruction of CVOCs. Besides, the catalytic reaction pathways of CVOCs over catalysts can provide an adequate understanding of the chemical reaction details, which would certainly help in the development of novel strategies for multi-catalytic reactions. Therefore, it would be better to give the catalytic reaction pathways and by-products distribution in the oxidation of CVOCs.

In this work, double-perovskite La_xSr_{2-x}MnCoO₆ materials with different Sr contents were prepared by the coprecipitation method, and LaSrMnCoO₆/H-ZSM-5 (LSMC/Z) catalysts with varied LaSrMnCoO₆ contents were further synthesized by the hydrothermal method using tetrapropylammonium hydroxide (TPAOH) as the structure-directing agent. The effects of the physicochemical properties of the synthesized materials on the catalytic activity, product selectivity, destruction mechanism, and reaction durability in 1,2-DCE destruction were investigated for the first time. The results indicated that the Sr content has an important influence on the catalytic activity of La_xSr_{2-x}MnCoO₆ materials in the oxidation of 1,2-DCE, and that LaSrMnCoO₆ possesses a higher catalytic activity than that of La₂MnCoO₆, La_{1.5}Sr_{0.5}MnCoO₆, and La_{0.5}Sr_{1.5}MnCoO₆. We found that the LaSrMnCoO₆/H-ZSM-5 composite materials have much better 1,2-DCE decomposition performance compared with LaSrMnCoO₆ and H-ZSM-5 owing to their possessing large amounts of surface adsorbed oxygen species, a high Mn⁴⁺/Mn³⁺ ratio, excellent chlorine resistance, and 1,2-DCE adsorption capability.

2. Experimental

2.1. Catalyst preparation

Preparation of La_xSr_{2-x}MnCoO₆. The double-perovskite La_xSr_{1-x}MnCoO₆ materials were synthesized using the coprecipitation method. Typically, 2.17 g of cetyltrimethylammonium bromide (CTAB) was totally dissolved in 200 mL of deionized water, and then stoichiometric amounts of LaJNO₃)₃·6H₂O (99.0%), SrJCH₃COO)₂·0.5H₂O (99.0%), MnJCH₃COO)₂·4H₂O (99.0%), and CoJNO₃)₂·6H₂O (99.0%) were dissolved in the solution (nCTAB/metal precursor = 0.75), which was kept stirring for 1 h. Then, a certain amount of NaOH (1 M) solution was added into the above solution (until the pH reached 13.0) and stirring was maintained for 12 h. Subsequently, the obtained solution was transferred into a Teflon container and was hydrothermally reacted at 90 °C for 3 h. The obtained precipitate was washed with distilled water and anhydrous ethanol three times, and the obtained powder was dried at 60 °C for 6 h. Finally, the resulting black powder was calcined at 500 °C for 3 h (heating rate of 6 °C min⁻¹) and 1100 °C for 3 h (heating rate of 6 °C min⁻¹) continuously under an air atmosphere to obtain La_xSr_{2-x}MnCoO₆.

Preparation of LaSrMnCoO₆/H-ZSM-5 and 10 wt% LaSrMnCoO₆ + H-ZSM-5. LaSrMnCoO₆/H-ZSM-5 (Si/Al = 300) materials were prepared by the hydrothermal method using tetrapropylammonium hydroxide (TPAOH) as the structure-directing agent. Typically, NaOH (1.38 g) and TPAOH (11.7 g) were dissolved in 71 mL of deionized water under stirring. Then, 15.9 g of H₂SiO₃ was added into the mixture, with stirring maintained for 1 h at room temperature. The obtained solution was transferred into a 100 mL of Teflon-lined autoclave and heated at 100 °C for 16 h to obtain TPAOH–Si. After that, NaOH (0.88 g) and NaAlO₂ (0.202 g) were dissolved in 87.6 mL of deionized water, and then 11.3 g of H₂SiO₃ and 5 g of TPAOH–Si were added into the mixed solution under

stirring. Next, a certain amount of prepared LSMC (weight ratio of LSMC/SiO₂ = 0.1, 0.2, 0.3, or 0.5) was added into the mixed solution, which was stirred for 1 h and then sealed in a Teflon-lined autoclave and heated at 180 °C for 40 h. After cooling to room temperature, the precipitate was washed with deionized water and dried at 100 °C for 24 h. The obtained solid was then added into 0.1 M of NH₄NO₃ solution for ion exchange under room temperature. Then, the precipitate was washed with deionized water and dried at 100 °C for 24 h. Finally, the resulting powder was calcined at 500 °C for 3 h (heating rate of 6 °C min⁻¹) under an air atmosphere to obtain the LaSrMnCoO₆/H-ZSM-5 materials, named as xLSMC/Z (x = 0.1, 0.2, 0.3, or 0.5). H-ZSM-5 material was prepared using the same synthetic route without the addition of LSMC. 10 wt% LaSrMnCoO₆ + H-ZSM-5 (0.1LSMC + Z, 10 wt% LaSrMnCoO₆ + 90 wt% H-ZSM-5) was prepared by a mechanical mixing method.

2.2. Catalyst characterizations

X-ray diffraction (XRD) patterns were performed on an X'Pert Pro powder diffraction system using Cu K α radiation (λ = 0.15418 nm) in the 2 θ range of 10–80° with ω scanning rate of 10° min⁻¹. Fourier transform infrared spectra (FT-IR) were recorded using a Bruker Tensor 37 spectrometer. Field-emission scanning electron microscopy (FE-SEM) images were obtained with a JEOL JSM-7800F microscope. High-resolution transmission electron microscopy (HR-TEM) was performed on an FEI Tecnai G2F30 microscope operating at an acceleration voltage of 300 kV. N₂ adsorption/desorption isotherms were conducted with an SSA-6000 gas sorption analyzer at -196 °C to measure the BET surface areas of the samples.

The chemical compositions of the samples were determined on a Kratos Axis Ultra DLD multifunctional X-ray photoelectron spectrometer (XPS). Binding energies (BE) were calibrated relative to the C 1s peak (284.8 eV) from adventitious carbon adsorbed on the surface of the samples. The temperature-programmed reduction of H₂ (H₂-TPR), temperature-programmed desorption of O₂ (O₂-TPD), temperature-programmed desorption of NH₃ (NH₃-TPD), and temperature-programmed desorption of 1,2-DCE (1,2-DCE-TPD) were performed on an automatic adsorption analyzer (TP-5080, Xianquan Co., China) equipped with a thermal conductivity detector (TCD). In a typical H₂-TPR experiment, the catalyst (100 mg) was pretreated at 400 °C for 30 min in the presence of N₂ with a flow of 40 mL min⁻¹ to remove the adsorbed CO₂ and H₂O before the H₂-TPR test. Then, the sample was further reduced under a 5 vol% H₂/Ar flow (30 mL min⁻¹) from 30 °C to 800 °C at a heating rate of 10 °C min⁻¹. Likewise, 100 mg of the sample was used in the O₂-TPD experiments. The sample was also pretreated in a N₂ flow (30 mL min⁻¹) at 400 °C for 30 min to remove the adsorbed CO₂ and H₂O. Next, the sample was treated in a 21 vol% O₂/N₂ flow at 35 °C for 30 min. Then, the sample was heated from 30 °C to 700 °C at a heating rate of 10 °C min⁻¹

in a pure N₂ stream. Also, 100 mg of the sample was used in the NH₃-TPD experiments (NH₃-TPD). Here, the sample was also pretreated in a N₂ flow (30 mL min⁻¹) at 300 °C for 30 min to remove the adsorbed CO₂ and H₂O. Next, the sample was treated in a 2.01 vol% N₂/NH₃ flow at 100 °C for 30 min. Then, the sample was heated from 100 °C to 800 °C at a heating rate of 10 °C min⁻¹ in a N₂ stream. Similarly, the temperature-programmed desorption of 1,2-DCE (1,2-DCE-TPD) was conducted the same as for the procedure for O₂-TPD with the automatic adsorption analyzer (1,2-DCE = 1000 ppm). Thermogravimetric analysis (TG) of the used catalysts was conducted on an HCT-2TGA/DSC-1 analyzer (Beijing Per-manent, China) from room temperature to 700 °C at a rate of 10 °C min⁻¹ under a continuous air flow of 50 mL min⁻¹.

2.3. Catalytic activity

The catalytic oxidation of 1,2-DCE was evaluated in a continuous flow quartz tube reactor (I.D. = 10 mm), in which the temperature was controlled by a K-type thermocouple placed in the catalyst bed. Here, 0.5 g of the sample (40–60 mesh) and 500 ppm of 1,2-DCE in a 400 mL min⁻¹ air stream (21 vol% O₂, N₂ balance) with a gas hourly space velocity (GHSV) of 48 000 mL g⁻¹ h⁻¹ were used in each test. The catalytic activities of La_xSr_{2-x}MnCoO₆ and LSMC/Z were measured in the temperature range of 200–550 °C and 200–580 °C, respectively. The 1,2-DCE conversion was calculated by the difference between the inlet and outlet 1,2-DCE concentrations. The reactants and reaction products were analyzed using an online gas chromatograph (GC9890) equipped with an electron capture detector (ECD) and flame ionization detector (FID), while a SHP8400PMS-L mass spectrometer (Sunny Hengping, China) equipped with a heated quartz inlet capillary was used to detect the gas phase species. The conversion of 1,2-DCE and the selectivity to CO, CO₂, HCl, and Cl₂ were calculated as follows:

$$\text{DCE conversion \%} = \frac{1,2\text{-DCE}_{\text{in}} - 1,2\text{-DCE}_{\text{out}}}{1,2\text{-DCE}_{\text{in}}} \times 100 \quad (1)$$

$$\text{CO selectivity \%} = \frac{\text{CO}_{\text{out}}}{2 \times \frac{1,2\text{-DCE}_{\text{in}} - 1,2\text{-DCE}_{\text{out}}}{1,2\text{-DCE}_{\text{in}}}} \times 100 \quad (2)$$

$$\text{CO}_2 \text{ selectivity \%} = \frac{\text{CO}_2_{\text{out}}}{2 \times \frac{1,2\text{-DCE}_{\text{in}} - 1,2\text{-DCE}_{\text{out}}}{1,2\text{-DCE}_{\text{in}}}} \times 100 \quad (3)$$

$$\text{Cl}_2 \text{ selectivity \%} = \frac{\text{Cl}_2_{\text{out}}}{2 \times \frac{1,2\text{-DCE}_{\text{in}} - 1,2\text{-DCE}_{\text{out}}}{1,2\text{-DCE}_{\text{in}}}} \times 100 \quad (4)$$

$$\text{HCl selectivity \%} = \frac{[\text{HCl}]_{\text{out}}}{[\text{HCl}]_{\text{in}}} \times 100 \quad (5)$$

where $[\text{1,2-DCE}]_{\text{in}}$ and $[\text{1,2-DCE}]_{\text{out}}$ are the inlet and outlet concentrations of 1,2-DCE, respectively, and $[\text{CO}]$, $[\text{CO}_2]$, $[\text{Cl}_2]$, and $[\text{HCl}]$ are the outlet concentrations of CO, CO₂, Cl₂, and HCl, respectively.

3. Results and discussion

3.1. Catalytic performance

The catalytic activities of the synthesized materials in the oxidation of 1,2-DCE are shown in Fig. 1. LaSrMnCoO₆ (LSMC) presented the best activity with T₅₀ and T₉₀ (the temperatures for 50% and 90% conversion of 1,2-DCE, respectively) temperatures of about 415 °C and 509 °C (Fig. 1A and Table S1†). Based on the T₉₀ temperature, the catalytic activity of La_xSr_{2-x}MnCoO₆ samples followed the sequence: LaSrMnCoO₆ (499 °C) > La₂MnCoO₆ (528 °C) > La_{1.5}Sr_{0.5}MnCoO₆ (533 °C)

> La_{0.5}Sr_{1.5}MnCoO₆ (537 °C). It can be concluded that the appropriate substitution of La element by Sr in the A site can improve the activity of double-perovskite materials, as the substitution of La³⁺ by Sr²⁺ induces a positive charge on Mn³⁺ and Co²⁺ (which tend to be oxidized to Mn⁴⁺ and Co³⁺), thereby enhancing the formation of anionic vacancies.¹⁷ LaSrMnCoO₆/H-ZSM-5 materials were further prepared with a target to improve the catalytic activity of LaSrMnCoO₆. The light-off curves of 1,2-DCE oxidation over LSMC/Z and H-ZSM-5 are displayed in Fig. 1B. The activity of LSMC/Z, H-ZSM-5, and 0.1LSMC/Z for 1,2-DCE destruction decreased in the order: 0.1LSMC/Z (T₉₀ = 337 °C) > 0.2LSMC/Z (T₉₀ = 358 °C) > 0.3LSMC/Z (T₉₀ = 370 °C) > 0.5LSMC/Z (T₉₀ = 386 °C) > H-ZSM-5 (T₉₀ = 411 °C) > 0.1LSMC + Z (T₉₀ = 422 °C). Compared with LSMC and H-ZSM-5, it could be observed that the catalytic activity of LSMC/Z materials was obviously increased. However, the activity of LSMC/Z composites decreased significantly with increasing the LSMC content, owing to partial aggregation and the lower dispersion of the LSMC phase. As displayed in Fig. 1B, it can be seen that the 0.1LSMC + Z material has the lowest catalytic activity compared to the LSMC/Z and H-ZSM-5 materials, suggesting that the synergy effect be-

tween LSMC and H-ZSM-5 plays an important positive role in 1,2-DCE destruction. The oxidation of 1,2-DCE over transition metal oxides is considered to follow a first-order reaction mechanism with respect to 1,2-DCE concentration (c): $r = -kc$
 $= (-A \exp(-E_a/RT))c$, where r is the reaction rate (mol s⁻¹), k is the rate constant (s⁻¹), A is the pre-exponential factor, and E_a is the apparent activation energy (kJ mol⁻¹). As shown in Fig. 1B and Table 1, 0.1LSMC/Z displayed the highest reaction rate of 11.82×10^{-8} mmol g⁻¹ s⁻¹ at 337 °C, which was respectively around 1.36 and 3.66 times higher than that over H-ZSM-5 (8.67 mmol g⁻¹ s⁻¹) and LSMC (3.23 mmol g⁻¹ s⁻¹), indicating that the introduction of H-ZSM-5 enhances the 1,2-DCE destruction efficiency of LSMC.

The selectivities of CO₂, CO, HCl, and Cl₂ in the oxidation of 1,2-DCE over La_xSr_{2-x}MnCoO₆ catalysts at 580 °C are displayed in Fig. 2A. LaSrMnCoO₆ possessed the best CO₂ selectivity (89.2%) and HCl selectivity (40.3%). The CO₂ selectivity over all the samples followed the order: LaSrMnCoO₆ (89.2%) > La₂MnCoO₆ (79.2%) > La_{0.5}Sr_{1.5}MnCoO₆ (68.2%) > La_{1.5}Sr_{0.5}MnCoO₆ (66.1%). Fig. 2B exhibits the selectivity of CO₂, CO, HCl, and Cl₂ during 1,2-DCE combustion over the 0.1LSMC/Z catalyst. It can be observed that the CO₂ selectivity clearly increases along with the increasing reaction temperature, while CO selectivity decreases at high temperature (>400 °C) as CO would be the further oxidized to CO₂ at elevated temperatures in the presence of active oxygen species.²⁴ The selectivity of HCl increases to 60% with increasing temperature, similar to CO₂ selectivity. Notably, Cl₂ selectivity appears to be stable below 400 °C but significantly increases above 400 °C, suggesting that the Deacon reaction (2HCl(g) + 0.5O₂ → H₂O(lg) + Cl₂(lg)) occurs when the temperature is higher than 400 °C, promoting the formation of Cl₂. The CO and CO₂ selectivities of LSMC/Z catalysts are shown in Fig. 2C.²⁵ It can be observed that CO₂ selectivity over the prepared materials decreases along with the increase in LSMC content, especially when the weight ratio of LSMC/SiO₂ was higher than 0.2.

3.2. By-products distribution and reaction path

The by-product type and distribution during 1,2-DCE decomposition over the prepared materials were studied, and the results revealed that vinyl chloride (VC), 1,1,2-trichloroethane (1,1,2-TCA), trichloroethylene (TCE), perchloroethylene (PCE), and acetaldehyde (ACE) were the primary intermediates in the temperature range 200–500 °C. The by-product distributions as a function of temperature are displayed in Fig. 3 and S2.† As shown in Fig. 3, the concentration of the chlorinated intermediates (1,1,2-TCA, TCE, and PCE) increases first with the increase in temperature and then decreases subsequently. The formation of ACE over the synthesized materials mainly occurred at 400–500 °C. It could be observed that the VC concentration over the 0.1LSMC/Z catalyst reached the maximum value at around 200 °C, and the formed VC could then be totally oxidized at 500 °C (Fig. S2†). As shown in Fig. 3A, 1,1,2-TCA was first detected at about 200 °C and reached the

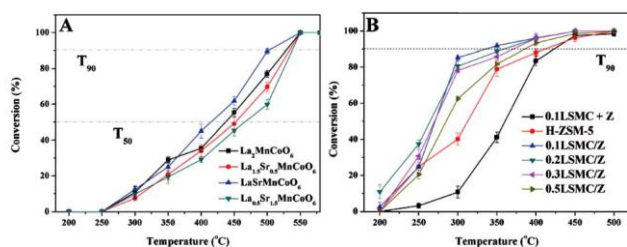


Fig. 1 Light-off curves of 1,2-DCE oxidation over: (A) La_{1-x}Sr_xMnCoO₆ and (B) LSMC/Z materials.

Table 1 Physicochemical properties and catalytic performance of the synthesized catalysts

Sample	S _{BET} ^a (m ² g ⁻¹)	D _V ^b (cm ³ g ⁻¹)	D _p ^c (nm)	T ₅₀ ^d (°C)	T ₉₀ ^d (°C)	r ₁ × 10 ^{-8e} (mmol g ⁻¹ s ⁻¹)
H-ZSM-5	296.4	0.05	4.48	308	411	8.67
LSMC	11.0	0.12	53.6	415	509	3.23
0.1LSMC/Z	96.3	0.10	21.1	263	337	11.82
0.2LSMC/Z	100.3	0.10	13.7	270	358	11.37
0.3LSMC/Z	52.9	0.09	13.3	270	370	10.96
0.5LSMC/Z	35.9	0.07	16.1	287	386	9.97

Note: ^a BET surface area calculated at P/P₀ = 0.05–0.25. ^b Total pore volume estimated at P/P₀ = 0.99. ^c BJH pore diameter calculated from the adsorption branch. ^d Temperatures at which 50% and 90% conversion of 1,2-DCE are achieved. ^e 1,2-DCE reaction rate gained at 337 °C.

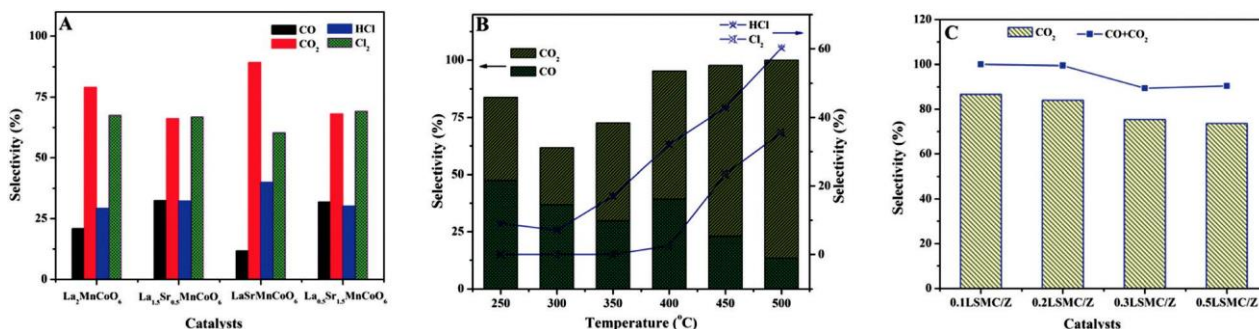


Fig. 2 (A) CO, CO₂, HCl, and Cl₂ distribution over synthesized La_{1-x}Sr_xMnCoO₆ catalysts at 580 °C; (B) selectivity of CO, CO₂, HCl, and Cl₂ over 0.1LSMC/Z; (C) CO and CO₂ selectivity of LSMC/Z at 500 °C.

maximum value at 400 °C due to the electrophilic addition reaction between VC and the electrophilic reagent HCl. Simultaneously, the formed 1,1,2-TCA further takes place in de-chlorination and/or a substitution reaction in the oxidation process (especially when the reaction temperature is higher than 350 °C), forming other chlorinated by-products. The concentration of 1,1,2-TCA over the prepared materials followed the order: 0.5LSMC/Z (226 ppm) > 0.3LSMC/Z (219 ppm) > 0.2LSMC/Z (98 ppm) > H-ZSM-5 (64 ppm) > 0.1LSMC/Z (25 ppm), indicating that the synergistic effect be-

tween LSMC and H-ZSM-5 could enhance the catalytic activity of LSMC and H-ZSM-5 and inhibit the formation of by-products in 1,2-DCE decomposition. Fig. 3B and C reveal that a certain amount of TCE and PCE was further formed through the decomposition of 1,1,2-TCA (300–400 °C) and by the dehydrochlorination of TCE (400–450 °C), respectively. ACE is one of the most common by-products in the oxidation of CVOCs over H-ZSM-5.²⁶ In our work, ACE could also be detected over the LSMC/Z and H-ZSM-5 materials when the reaction temperature was higher than 400 °C, as shown in Fig. 3D. It could be observed that the 0.1LSMC/Z catalyst possessed the lowest ACE concentration, and the concentration of ACE over the LSMC/Z materials increased with the increasing weight ratio of LSMC.

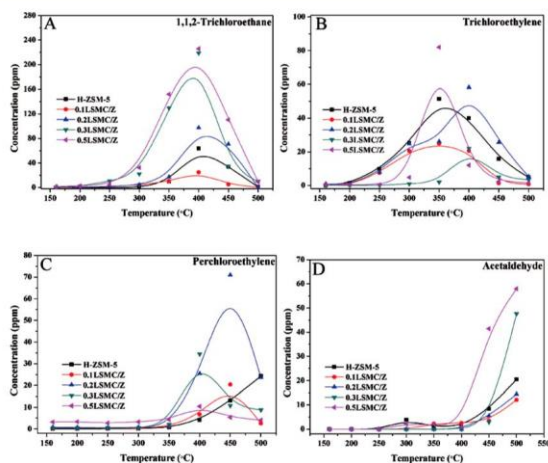
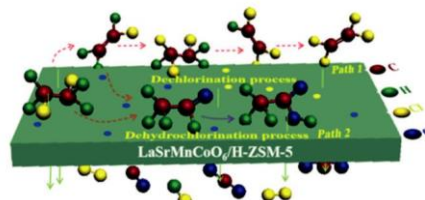


Fig. 3 The 1,1,2-trichloroethane (A), trichloroethylene (B), perchloroethylene (C), and acetaldehyde (D) distribution at the temperature range of 160–500 °C.

The proposed oxidation routes for 1,2-DCE based on the above results are displayed in Scheme 1. Here, C–Cl with a lower bond energy (328 KJ mol⁻¹) than that of C–C (332 KJ mol⁻¹) is easier attacked in the oxidation process. Therefore,



Scheme 1 The proposed mechanism for 1,2-DCE oxidation over LSMC/Z materials.

the cleavage of C–Cl is the key step in the oxidation of 1,2-DCE. As shown in Scheme 1, the formation of ACE is probably ascribed to the partial dechlorination of VC or 1,2-DCE, which results from the attack of oxygen species and the formation of carbonyl species. Afterwards, the following oxygen attack results in the yield of CHCl_2CHO or acetic acid, which was not detected in the oxidation process due to its higher generation temperature or due to their relatively low concentration. Additionally, C–Cl bond cleavage can promote the formation of 1,1,2-TCA. The next dehydrochlorination and decomposition of 1,1,2-TCA would facilitate the formation of TCE and PCE. Finally, the chlorinated by-products are almost oxidized to CO , CO_2 , HCl , and Cl_2 by the chemically adsorbed oxygen species (O_2^- and O^-) at about 500 °C.

3.3. Catalytic stability and coke formation

The catalytic stability of the typical used materials (0.1LSMC, H-ZSM-5, and LSMC) in the oxidation of 1,2-DCE were studied, as displayed in Fig. 4. It could be observed that LSMC performed with good stability at 500 °C, due to the excellent structure stability of the double-perovskite-type oxide. The conversion of 1,2-DCE over H-ZSM-5 reduced gradually from the beginning of the reaction up to 267 min, and an obvious reduction of 1,2-DCE conversion (from 90% to 63%) could be observed when the reaction time was increased further, indicating that coke formation and chlorine species attack cause the deactivation of H-ZSM-5.²⁷ The catalytic stability of 0.1LSMC/Z was much better than that of H-ZSM-5, over which no obvious reduction of 1,2-DCE conversion could be found within 517 min and the final conversion of 1,2-DCE could be maintained at around 80%, suggesting that LSMC, with its excellent structural stability, could enhance the chlorine resistance and inhibit carbon deposition over the LSMC/Z materials.

TG-DTA was conducted to determine the amount of coke deposited on the used catalysts, as shown in Fig. 5. All the TG curves could be divided into three regions. The first stage in the temperature range of 30–200 °C could be assigned to the loss of molecular water, adsorbed water, and adsorbed organisms.^{28,29} No obvious weight loss of the catalysts could be found in the second stage within the temperature range 200–

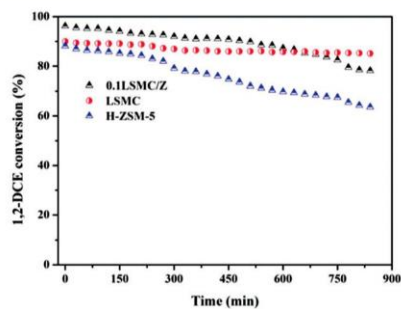


Fig. 4 Stability of LSMC (500 °C) and 0.1LSMC/Z and H-ZSM-5 for 1,2-DCE oxidation at 400 °C.

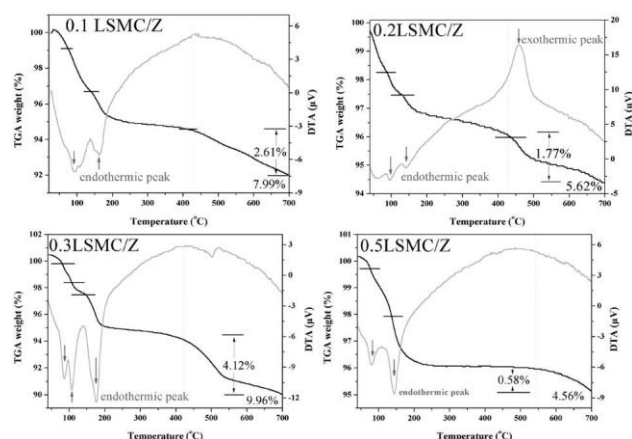


Fig. 5 TG-DTA profiles of 0.1LSMC/Z, 0.2LSMC/Z, 0.3LSMC/Z, and 0.5LSMC/Z.

400 °C. Distinct exothermic processes could then be detected in the temperature range 400–700 °C (the third stage) due to the decomposition of carbon deposits.³⁰ It could be observed that the weight ratio of the coke over the catalyst followed the order: 0.5LSMC/Z (0.58%) < 0.2LSMC/Z (1.77%) < 0.1LSMC/Z (2.61%) < 0.3LSMC/Z (4.12%). 0.5LSMC/Z showed the lowest amount of coke due to the superior carbon deposition resistance of the double perovskite, in good agreement with the stability test (Fig. 4). On the contrary, 0.3LSMC/Z showed the largest amount of coke deposits, while the amount of coke deposits over 0.2LSMC/Z and 0.1LSMC/Z were lower than that over 0.3LSMC/Z, attributed to their higher activity, indicating that 0.3LSMC/Z could be attacked more easily by the formation of coke.

3.4. Structural, morphological, and textural properties

The crystalline structure of the synthesized materials was characterized by XRD, as displayed in Fig. S1† and 6. As shown in Fig. S1,† the synthesized $\text{La}_x\text{Sr}_{2-x}\text{MnCoO}_6$ catalysts showed typical diffraction peaks of double perovskites at 2θ of 23.0°, 32.8°, 36.7°, 40.5°, 46.8°, 58.6°, and 68.9°, illustrating

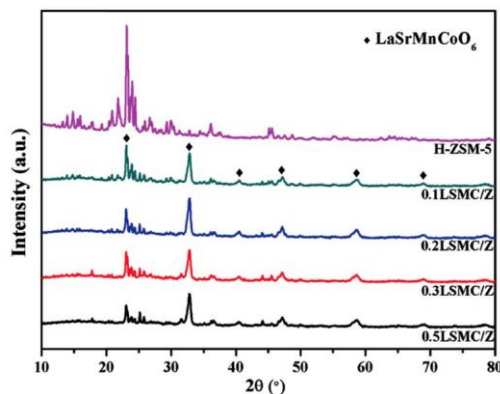


Fig. 6 XRD patterns of the synthesized materials.

the successful synthesis of double-perovskite-type oxides. All LSMC/Z catalysts possessed typical diffraction peaks of double perovskites, confirming that the LaSrMnCoO_6 phase was successfully formed and incorporated to H-ZSM-5 in the hydro-thermal method. It is worth noting that all the LSMC/Z materials exhibited similar diffraction patterns to that of H-ZSM-5, suggesting that the introduction of LSMC had an insignificant effect on the structure of the H-ZSM-5 support.

FT-IR spectra of all the prepared materials are displayed in Fig. 7. It was found that all the LSMC/Z materials had similar structural features. The bands at 1232, 1100, 548, and 450 cm^{-1} are the characteristic absorption peaks of H-ZSM-5.³¹ In particular, the band at 548 cm^{-1} in the spectra of all the samples is related to the vibration of the five-membered oxygen rings of the H-ZSM-5 skeleton structure, while the decrease of the peak intensity after the introduction of the LSMC phase indicates the loss of crystallinity, which is in agreement with the XRD results.³² The bands at 1100 and 800 cm^{-1} are associated with the asymmetric and symmetric stretching vibrations of Si-O-Si, Si-O-Al or Al-O-Al, while

the band at 450 cm^{-1} is ascribed to the vibration of Si-O or Al-O in the SiO_4 and AlO_4 tetrahedrons.^{31,33} It could be also detected that the intensities of the bands at 1100, 800, and 450 cm^{-1} were slightly decreased with the increase in LSMC loadings, which indicated that the addition of LSMC may weaken the vibration of the bonds in the skeleton structure of H-ZSM-5, which is in accordance with the XRD results (Fig. 6). The bands at 855 and 1465 cm^{-1} were only detected in the spectra of LSMC/Z materials, which is respectively related to the CO_3^{2-} and C-H bending vibrations (Fig. 8).^{34,35}

Fig. 8 shows the typical SEM images of the prepared samples. The H-ZSM-5 sample possessed a uniform hexagonal columnar crystal morphology with a length of ca. $1.5\text{ }\mu\text{m}$, while a similar morphology could also be found over the 0.1LSMC/Z and 0.2LSMC/Z materials. However, the 0.3LSMC/Z and 0.5LSMC/Z samples showed an irregular morphology, which was different from that of H-ZSM-5, suggesting that higher loadings may cause a partial aggregation of the catalyst. The structures of the samples were further demonstrated by the TEM and STEM patterns, as

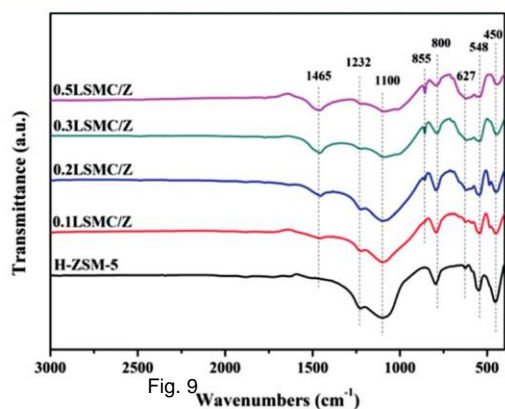


Fig. 7 FT-IR profiles of the prepared catalysts.

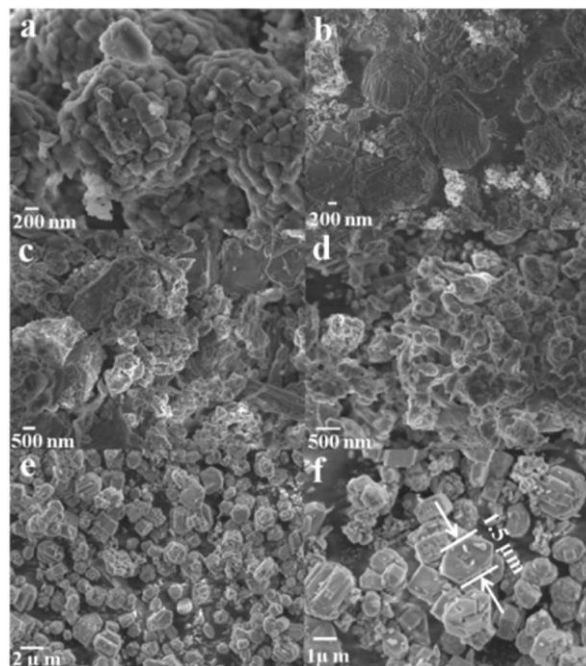
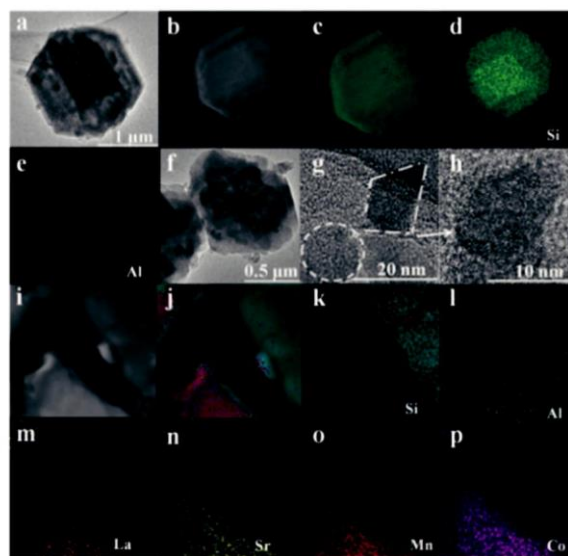


Fig. 8 FE-SEM images of: (a) 0.1LSMC/Z, (b) 0.2LSMC/Z, (c) 0.3LSMC/Z, (d) 0.5LSMC/Z, and (e and f) H-ZSM-5.

shown in Fig. 9. H-ZSM-5 (Fig. 9a and b) exhibited a hexagonal columnar morphology, corresponding well to the SEM results (Fig. 8e and f). STEM-EDX was conducted to evaluate the integrated intensity of the elements of the materials. It could be distinctly observed that the Si and Al elements of H-ZSM-5 were dispersed homogeneously in the sample (Fig. 9c-e). The TEM of 0.1LSMC/Z displayed that LSMC was successfully loaded on the surface of H-ZSM-5 (Fig. 9f and g), and the crystalline interplanar



(a) HR-TEM and (b) STEM images of H-ZSM-5; (c-e) EDX elemental mappings of H-ZSM-5; (f-h) HR-TEM and (i) STEM images of 0.1LSMC/Z; (j-p) EDX elemental mappings of 0.1LSMC/Z.

spacing in Fig. 9h) was associated with the LSMC oxides. It could also be observed that the elements of Si, Al, La, Sr, Mn, and Co were dispersed homogeneously over the cata-lysts (Fig. 9j–p).

The textural properties of the prepared catalysts were determined by low-temperature nitrogen adsorption–desorption measurements. As shown in Fig. 10A, the samples exhibited a sharp increase at $P/P_0 = 0–0.1$, indicating the existence of large amounts of micropores.³⁰ Moreover, the amounts of micropores of the samples decreased with increasing the LSMC loading weight, indicating that the loading of LSMC influences the formation of micropores. The synthesized H-ZSM-5 displayed a type IV isotherm with a remarkable H4-type hysteresis loop at $P/P_0 = 0.4–0.9$, which could be associated with the existence of mesopores.³⁶ Moreover, all the LSMC/Z materials exhibited type IV isotherms, while the hysteresis loops were much smaller than that of H-ZSM-5, indicating that the incorporation of the LSMC phase can also hinder the formation of mesopores. The textural properties of the synthesized catalysts are summarized in Table 1, which also shows that the BET surface areas of all the materials followed the order: H-ZSM-5 ($296.4 \text{ m}^2 \text{ g}^{-1}$) > 0.2LSMC/Z ($100.3 \text{ m}^2 \text{ g}^{-1}$) > 0.1LSMC/Z ($96.3 \text{ m}^2 \text{ g}^{-1}$) > 0.3LSMC/Z ($52.9 \text{ m}^2 \text{ g}^{-1}$) > 0.5LSMC/Z ($35.9 \text{ m}^2 \text{ g}^{-1}$). The 0.2LSMC/Z sample possessed the highest specific surface area within the series of LSMC/Z materials, attributed to the existence of lots of mesopores in the 0.2LSMC/Z material. The reduction of the BET surface area of the LSMC/Z materials can be ascribed to the negative effect of LSMC species on the porosity of H-ZSM-

5 (which inhibits the formation of micro- and mesopores and blocks the pore channels).^{32,36} The pore size distribution curves of the prepared samples are depicted in Fig. 10B. It can be observed that all the catalysts have obvious peaks centered at 3.8 nm, illustrating the existence of a mesoporous structure. The BJH pore diameters of all the materials are listed in Table 1, and it can be seen that the pore diameter is enlarged after loading LSMC due to the formation of stacking holes, which also corresponds to the results from N_2 adsorption–desorption at $P/P_0 = 0.9–1.0$ (Fig. 9).

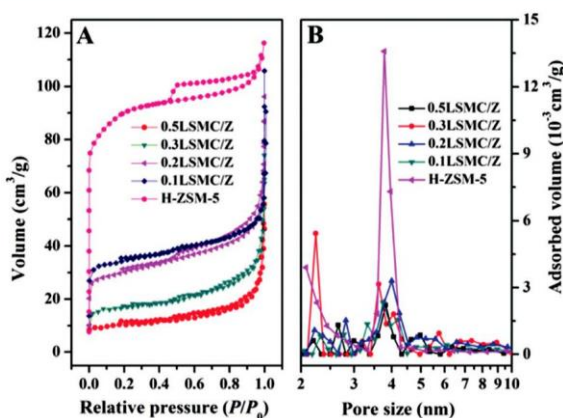


Fig. 10 (A) Nitrogen adsorption–desorption isotherms and (B) pore size distribution of all the catalysts.

3.5. Surface composition and element status

XPS was conducted to investigate the chemical state of the elements and the surface atomic concentration in the near-surface region of the synthesized catalysts. La 3d, Sr 3d, Mn 2p, Co 2p, and O 1s were analyzed with deconvolution by fitting a Gaussian–Lorentzian (GL) function with a Shirley background, as shown in Fig. 11. La 3d showed two doublets of peaks, corresponding to La 3d_{5/2} and La 3d_{3/2} associated with La³⁺ in the perovskite.³⁷ La 3d_{5/2} could be fitted into two peaks located at 834.7 and 837.7 eV, while two main peaks of La 3d_{3/2} occurred at 850.7 and 854.8 eV. The Sr 3d peaks located at 131.8 and 134.1 eV were related to Sr²⁺, while two binding energies (BEs) at 133.2 and 133.4 eV were associated with the presence of SrO.³⁸ The peaks at 133.7, 135.2, and 135.5 eV were attributed to SrCO₃.³⁹

The Co 2p XPS spectra of the samples exhibited two peaks at 779.7–780.2 and 795.1–795.9 eV, corresponding to Co 2p_{3/2} and Co 2p_{1/2}, respectively. However, Co²⁺ and Co³⁺ in the Co 2p spectra are hard to distinguish due to the small differences in their binding energy values and peak shapes.⁴⁰ According to the literature, the binding energies of the 2p level of 779.7–780.2 eV with the difference between Co 2p_{3/2} and Co 2p_{1/2} of about 15.4–15.8 eV are ascribed to the octahedral Co³⁺ component of Co₃O₄ over the catalyst.⁴¹ Also, the binding energies of the 2p level of 795.1–795.9 eV correspond to the Co²⁺ of Co₃O₄ in the catalyst.⁴²

The XPS spectra of Mn 2p also displayed two distinct peaks, corresponding to Mn 2p_{3/2} and Mn 2p_{1/2} with a spin–

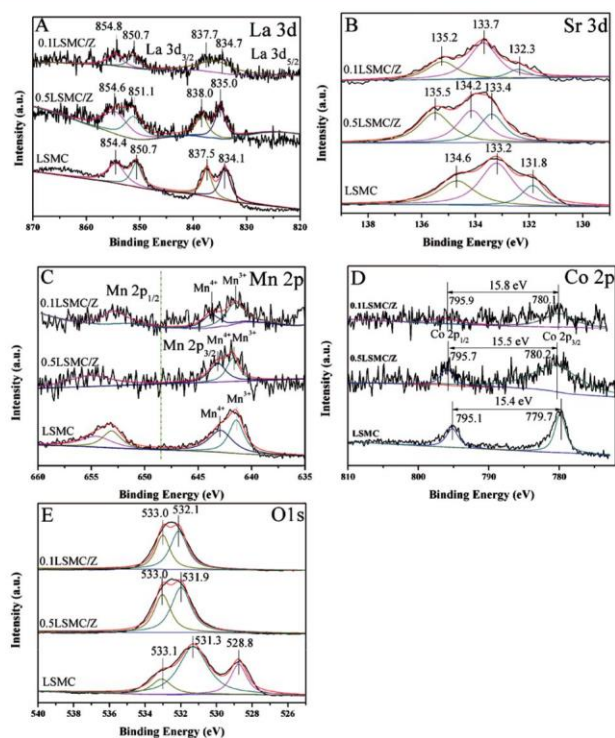


Fig. 11 (A) La 3d, (B) Sr 3d (C) Mn 2p, (D) Co 2p, and (E) O 1s XPS spectra of typical catalysts.

Table 2 XPS results of Mn 2p, Co 2p, and O 1s

Sample	Mn 2p _{3/2}			O 1s			
	Mn ⁴⁺	Mn ³⁺	Mn ⁴⁺ /Mn ³⁺	O _α ^a	O _β ^b	O _γ ^c	O _β /(O _α +O _β +O _γ)
0.1LSMC/Z	643.3	642.0	1.04	533.0	532.1	—	1.34
0.5LSMC/Z	643.2	641.8	0.85	533.0	531.9	—	1.25
LSMC	643.0	641.4	0.96	533.1	531.3	528.8	0.44

Note: ^a O_α represents adsorbed oxygen from the hydroxyl species and adsorbed water species. ^b O_β represents surface adsorbed oxygen species.

^c O_γ represents lattice oxygen.

orbit splitting value of 11.8 eV (Fig. 11C). The main spectra of Mn 2p_{3/2} could be divided into two peaks at around 641.4–

641.7 and 643.0–644.1 eV, which were associated with the Mn⁴⁺ and Mn³⁺ of LSMC, respectively.^{43,44} After the curve-fitting analysis of Mn 2p_{3/2}, the ratio between Mn⁴⁺ and Mn³⁺ species was calculated by their peak areas, which are presented in Table 2. The ratio of Mn⁴⁺/Mn³⁺ over 0.1LSMC/Z (1.04) was higher than that of LSMC (0.96) and 0.5LSMC/Z

(0.85), indicating that part of the Mn³⁺ in the LSMC is converted to Mn⁴⁺ in the synthesis process and that there is a larger amount of manganese vacancies in 0.1LSMC/Z.^{45,46}

The O 1s spectrum of LSMC showed three peaks with binding energies of 528.8, 531.3, and 533.1 eV, which were associated with the lattice oxygen (O²⁻), surface adsorbed oxygen species (physical adsorption oxygen (O₂), chemically adsorbed oxygen (O₂⁻), oxygen adsorbed on oxygen vacancies (O⁻)), and the adsorbed oxygen from the hydroxyl species/ adsorbed water species, respectively.^{3,47,48} The O 1s spectra of 0.1LSMC/Z and 0.5LSMC/Z just exhibited two peaks at 531.9–532.1 eV and 533.0 eV, suggesting that the concentration of lattice oxygen species over 0.1LSMC/Z and 0.5LSMC/Z is much lower than that of LSMC. The quantitative analysis of the O 1s spectra is listed in Table 2 in terms of O_β/(O_α+O_β+O_γ) (surface adsorbed oxygen species/total oxygen species). It can be found that the amounts of surface adsorbed oxygen over 0.1LSMC/Z (O_β/(O_α+O_β+O_γ) = 1.34) and 0.5LSMC/Z (O_β/(O_α+O_β+O_γ) = 1.25) are remarkably higher than that of LSMC (O_β/(O_α+O_β+O_γ) = 0.44). It is reported that a high concentration of surface adsorbed oxygen and metal ions with high oxidation states (such as Mn⁴⁺ and Co³⁺) over a catalyst are beneficial to its catalytic ability, and can play a key role in promoting the oxidation process.⁴⁹

3.6. Reducibility, oxygen species, and acid properties

H₂-TPR experiments were conducted to investigate the reducibility of the synthesized materials, as displayed in Fig. 12A. All the prepared materials possessed two reduction peaks centered at a temperature range of 455–470 °C and 620–649 °C, while the 0.1LSMC/Z catalyst had a small low-temperature peak at around 225 °C due to the reduction of surface chemically adsorbed oxygen species and the oxygen adsorbed at the oxygen vacancies.¹ The peaks of the synthesized materials centered at the temperature range 455–470 °C could be attributed to the reduction of MnO_x (MnO₂ →

Mn₂O₃ → Mn₃O₄) and CoO_x (Co₃O₄ → CoO → Co⁰).^{50,51} And the peaks above 600 °C could be attributed to the reduction of Mn₃O₄ (Mn₃O₄ → MnO) and CoO (CoO → Co⁰).⁵² The above reduction processes over the prepared materials can facilitate oxygen adsorption and promote electron transfer, and thus accelerate the 1,2-DCE oxidation rate.⁴²

O₂-TPD has been proved to be a useful technology to distinguish the active oxygen species over catalysts, as shown in Fig. 12B.

The active oxygen species can be divided into four types: physically adsorbed oxygen (O₂ (ads)), chemically adsorbed oxygen (O₂⁻ (ads)), oxygen adsorbed species on vacancies (O⁻ (ads)), and lattice oxygen (O²⁻).⁴⁷ It is reported that the adsorbed oxygen generally changes in the following procedures: O₂ (ads) → O₂⁻ (ads) → O⁻ (ads) → O²⁻ (lattice).⁴⁰ As shown in the O₂-TPD profiles, all the catalysts displayed two types of oxygen species with desorption temperatures around 60–77 °C and 464–487 °C. The first peak can be ascribed to the physically adsorbed oxygen (O₂) and chemically adsorbed

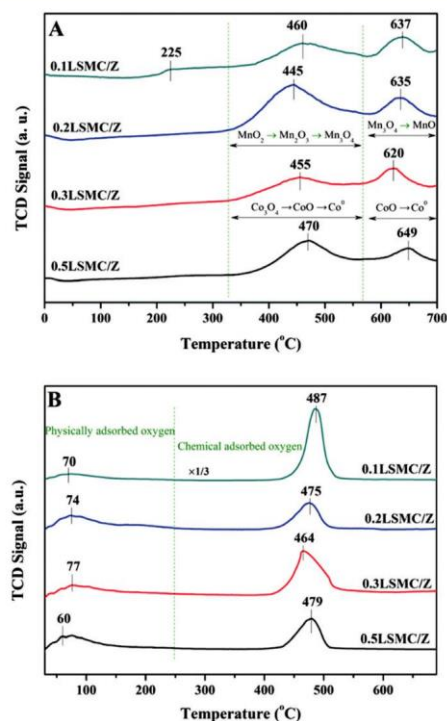


Fig. 12 (A) H₂-TPR and (B) O₂-TPD profiles of the prepared catalysts.

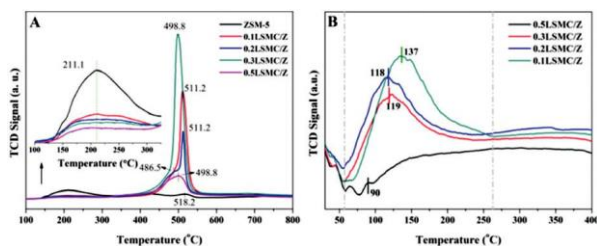


Fig. 13 (A) NH_3 -TPD profiles and (B) 1,2-DCE-TPD of the synthesized catalysts.

oxygen (O_2^- (ads)), which can be desorbed from the catalyst surface easier.⁴¹ The peaks located at the temperature range 300–750 °C can be associated with the desorption of the chemically adsorbed oxygen on the vacancies, corresponding to the second peak in this work.⁵³ Lattice oxygen species (O^{2-}) were not detected in this work because the desorption of lattice oxygen usually happens above 700 °C.⁵⁴ Obviously, 0.1LSMC/Z possessed the largest amount of chemically adsorbed oxygen species among 0.2LSMC/Z, 0.3LSMC/Z, and 0.5LSMC/Z materials, which can take part in the oxidation process and accelerate the overall destruction speed for 1,2-DCE.

The acid properties of the catalysts have a significant influence on the 1,2-DCE destruction process.¹⁰ In a typical oxidation process, 1,2-DCE is first adsorbed on the Lewis acid sites, resulting in the formation of the main by-products VC by dehydrochlorination because of the effect of active oxygen species over the catalysts.^{5,10,55} Then, the further dechlorination reaction occurs to form other chlorinated by-products. Temperature-programmed desorption of NH_3 is an efficient technology to evaluate the acid properties of the prepared materials, and the profiles from this are shown in Fig. 13A. Two main peaks can be clearly observed at 211 °C and 480–520 °C, which can be, respectively, attributed to the catalyst weak acid sites and strong acid sites.⁵⁶ The weak acid sites at low temperature are associated with the desorption of ammonia from the Lewis acid sites and the strong acid sites at high temperature corresponded to the desorption of ammonia from the Brønsted acid sites.⁵⁷ As shown in Fig. 13A, the intensity of the peaks of LSMC/Z at 211 °C follows the sequence: 0.1LSMC/Z > 0.2LSMC/Z > 0.3LSMC/Z > 0.5LSMC/Z, which is in accordance with the order of catalytic activity. ZSM-5 with the most Lewis acid sites possessed the lowest catalytic activity compared to LSMC/Z on account of the absence of active contents. In the temperature range 480–520 °C, the intensity of the strong acid sites over LSMC/Z could be detected in the order: 0.3LSMC/Z > 0.1LSMC/Z > 0.2LSMC/Z > 0.5LSMC/Z. According to previous studies, the existence of CO- and Cl-containing by-products in the oxidation process, even at high temperatures, can cause severe de-activation (mainly caused by coke), due to the strong acid property of zeolites.²⁹ 0.3LSMC/Z with the largest amount of strong acid sites are considered to be attacked more easily by the formation of coke, which could be determined by the TG

results (Fig. 5). Notably, the amount of coke over the used catalysts had a great positive correlation with the amount of strong acid sites.

Fig. 13B shows the 1,2-DCE adsorption/desorption performances over the prepared LSMC/Z materials. In general, the higher desorption temperature of 1,2-DCE indicates the stronger adsorption between VOC molecules and active sites over the catalyst.⁵⁸ The 1,2-DCE adsorption is one of the most important steps in the 1,2-dichloroethane oxidation process. It can be observed that the corresponding desorption temperatures of 1,2-DCE over the catalysts were as follows: 0.1LSMC/Z (137 °C) > 0.3LSMC/Z (119 °C) > 0.2LSMC/Z (118 °C) > 0.5LSMC/Z (90 °C), suggesting that the 1,2-DCE molecules were stronger adsorbed over 0.1LSMC/Z than over 0.3LSMC, 0.2LSMC/Z, and 0.5LSMC/Z. The desorption peak areas correspond to the 1,2-DCE adsorption capacity of the samples. As shown in Fig. 13B, the desorption peak areas of 1,2-DCE follow the sequence: 0.1LSMC/Z > 0.2LSMC/Z > 0.3LSMC/Z > 0.5LSMC/Z, illustrating that 0.1LSMC/Z possessed the largest 1,2-DCE adsorption capacity, which promotes the oxidation process of 1,2-DCE.

4. Conclusions

$\text{La}_x\text{Sr}_{2-x}\text{MnCoO}_6$ materials with different Sr contents were investigated in 1,2-DCE oxidation. The results suggested that the Sr content in $\text{La}_x\text{Sr}_{2-x}\text{MnCoO}_6$ has a significant influence on the catalytic activity and that LaSrMnCoO_6 possessed the highest activity among all the $\text{La}_x\text{Sr}_{2-x}\text{MnCoO}_6$ catalysts. H-ZSM-5, with a large surface area and abundant acid sites, was further introduced via a hydrothermal process to improve the performance of LaSrMnCoO_6 , and the results revealed that the $\text{LaSrMnCoO}_6/\text{H-ZSM-5}$ materials had much higher catalytic activity for 1,2-DCE oxidation than that of LaSrMnCoO_6 and H-ZSM-5 due to the larger specific surface area, higher concentration of high-valence manganese and cobalt species, better reducibility and oxygen mobility, and higher 1,2-DCE adsorption capacity. 10 wt% $\text{LaSrMnCoO}_6/\text{H-ZSM-5}$ possessed the best activity and selectivity in 1,2-DCE oxidation. Two reaction pathways (dechlorination and dehydrochlorination) over $\text{LaSrMnCoO}_6/\text{H-ZSM-5}$ for 1,2-DCE oxidation were proposed and several reaction by-products (vinyl chloride, 1,1,2-trichloroethane, trichloroethylene, tetrachloroethylene, and acetaldehyde) were detected, which are totally oxidized to the main oxidation products (CO_2 , CO, HCl, and Cl_2) at elevated temperatures.

Conflicts of interest

There are no conflicts to declare.

Acknowledgements

The authors thank the financial support from the National Natural Science Foundation of China (21477095, 21677114, 21337003), and the Fundamental Research Funds for the Central Universities (xjj2017170).

References

- 1 Q. Dai, W. Wang, X. Wang and G. Lu, *Appl. Catal.*, B, 2017, 203, 31–42.
- 2 C. Zhang, C. Wang, S. Gil, A. Boreave, L. Retailliau, Y. Guo, J. L. Valverde and A. Giroir-Fendler, *Appl. Catal.*, B, 2017, 201, 552–560.
- 3 C. He, Y. Yu, L. Yue, N. Qiao, J. Li, Q. Shen, W. Yu, J. Chen and Z. Hao, *Appl. Catal.*, B, 2014, 147, 156–166.
- 4 Y. I. Bauman, I. V. Mishakov, D. V. Korneev, Y. V. Shubin, A. A. Vedyagin and R. A. Buyanov, *Catal. Today*, 2018, 301, 147–152.
- 5 Q. Dai, S. Bai, H. Li, W. Liu, X. Wang and G. Lu, *Appl. Catal.*, B, 2015, 168–169, 141–155.
- 6 T. Chang, Z. Shen, Y. Huang, J. Lu, D. Ren, J. Sun, J. Cao and H. Liu, *Chem. Eng. J.*, 2018, 348, 15–25.
- 7 Y. I. Bauman, S. S. Sigaeva, I. V. Mishakov, A. A. Vedyagin, P. G. Tsyrlunikov, D. V. Korneev and R. A. Buyanov, *React. Kinet., Mech. Catal.*, 2017, 120, 691–701.
- 8 Y. I. Bauman, I. V. Mishakov, D. V. Korneev, Y. V. Shubin, A. A. Vedyagin and R. A. Buyanov, *Catal. Today*, 2018, 301, 147–152.
- 9 Q. Dai, L.-L. Yin, S. Bai, W. Wang, X. Wang, X.-Q. Gong and G. Lu, *Appl. Catal.*, B, 2016, 182, 598–610.
- 10 Z. Shi, P. Yang, F. Tao and R. Zhou, *Chem. Eng. J.*, 2016, 295, 99–108.
- 11 H. Pan, Y. Jian, Y. Yu, C. He, Z. Shen and H. Liu, *Appl. Surf. Sci.*, 2017, 401, 120–126.
- 12 C. He, B.-T. Xu, J.-W. Shi, N.-L. Qiao, Z.-P. Hao and J.-L. Zhao, *Fuel Process. Technol.*, 2015, 130, 179–187.
- 13 J. González-Prior, R. López-Fonseca, J. I. Gutiérrez-Ortiz and B. de Rivas, *Appl. Catal.*, B, 2016, 199, 384–393.
- 14 P. Yang, S. Yang, Z. Shi, Z. Meng and R. Zhou, *Appl. Catal.*, B, 2015, 162, 227–235.
- 15 P. Yang, X. Xue, Z. Meng and R. Zhou, *Chem. Eng. J.*, 2013, 234, 203–210.
- 16 C. Li, W. Wang, C. Xu, Y. Liu, B. He and C. Chen, *J. Nat. Gas Chem.*, 2011, 20, 345–349.
- 17 S. Royer, D. Duprez, F. Can, X. Courtois, C. Batiot-Dupeyrat, S. Laassiri and H. Alamdari, *Chem. Rev.*, 2014, 114, 10292–10368.
- 18 J. Kuhn and U. Ozkan, *J. Catal.*, 2008, 253, 200–211.
- 19 H. Arandiyan, H. Dai, J. Deng, Y. Liu, B. Bai, Y. Wang, X. Li, S. Xie and J. Li, *J. Catal.*, 2013, 307, 327–339.
- 20 C. Zhang, C. Wang, W. Hua, Y. Guo, G. Lu, S. Gil and A. Giroir-Fendler, *Appl. Catal.*, B, 2016, 186, 173–183.
- 21 A. Fu, A. Guan, F. Gao, X. Zhang, L. Zhou, Y. Meng and H. Pan, *Opt. Laser Technol.*, 2017, 96, 43–49.
- 22 V. L. Vilesh and G. Subodh, *Ceram. Int.*, 2017, 43, 12718–12723.
- 23 M. K. Rath and K.-T. Lee, *J. Alloys Compd.*, 2018, 737, 152–159.
- 24 M. Tian, C. He, Y. Yu, H. Pan, L. Smith, Z. Jiang, N. Gao, Y. Jian, Z. Hao and Q. Zhu, *Appl. Catal.*, A, 2018, 553, 1–14.
- 25 P. Yang, S. Zuo, Z. Shi, F. Tao and R. Zhou, *Appl. Catal.*, B, 2016, 191, 53–61.
- 26 J. Zheng, J. Liu, Z. Zhao, J. Xu, A. Duan and G. Jiang, *Catal. Today*, 2012, 191, 146–153.
- 27 N. Blanch-Raga, A. E. Palomares, J. Martínez-Triguero and S. Valencia, *Appl. Catal.*, B, 2016, 187, 90–97.
- 28 C. J. Van Oers, W. J. J. Stevens, E. Bruijn, M. Mertens, O. I. Lebedev, G. Van Tendeloo, V. Meynen and P. Cool, *Microporous Mesoporous Mater.*, 2009, 120, 29–34.
- 29 P. Yang, S. Zuo and R. Zhou, *Chem. Eng. J.*, 2017, 323, 160–170.
- 30 C. Chen, Y. Yu, C. He, L. Wang, H. Huang, R. Albilali, J. Cheng and Z. Hao, *Appl. Surf. Sci.*, 2018, 439, 113–121.
- 31 C. Zuo, T. Ge, X. Guo, C. Li and S. Zhang, *Microporous Mesoporous Mater.*, 2018, 256, 58–66.
- 32 Y. Hu, J. Liu, J. Cheng, L. Wang, L. Tao, Q. Wang, X. Wang and P. Ning, *Appl. Surf. Sci.*, 2018, 427, 843–850.
- 33 D. Li, J. Yao, H. Sun, B. Liu, S. van Agtmaal and C. Feng, *Appl. Surf. Sci.*, 2018, 427, 288–297.
- 34 G. Liu, L. Sun, J. Liu, F. Wang and C. J. Guild, *Mol. Catal.*, 2017, 440, 148–157.
- 35 G. A. Guirgis, S. Bell, H. Deeb, C. Zheng and J. R. Durig, *J. Mol. Struct.*, 2004, 706, 141–152.
- 36 S. Asadi, L. Vafi and R. Karimzadeh, *Microporous Mesoporous Mater.*, 2018, 255, 253–260.
- 37 J. M. Giraudon, A. Elhachimi, F. Wyrwalski, S. Siffert, A. Aboukais, J. F. Lamonier and G. Leclercq, *Appl. Catal.*, B, 2007, 75, 157–166.
- 38 K. Kim, J. Jeong, A. K. Azad, S. B. Jin and J. H. Kim, *Appl. Surf. Sci.*, 2016, 365, 38–46.
- 39 R. Tang, C. Jiang, Y. Fang and H. Yang, *Mater. Technol.*, 2016, 30, A181–A185.
- 40 P. Li, C. He, J. Cheng, C. Y. Ma, B. J. Dou and Z. P. Hao, *Appl. Catal.*, B, 2011, 101, 570–579.
- 41 T. Cai, H. Huang, W. Deng, Q. Dai, W. Liu and X. Wang, *Appl. Catal.*, B, 2015, 166–167, 393–405.
- 42 T. Zhou, T. Zhang, R. Zhang, Z. Lou, J. Deng and L. Wang, *Appl. Surf. Sci.*, 2017, 426, 951–956.
- 43 H. Pan, Y. Jian, C. Chen, C. He, Z. Hao, Z. Shen and H. Liu, *Environ. Sci. Technol.*, 2017, 51, 6288–6297.
- 44 Y. Liao, M. Fu, L. Chen, J. Wu, B. Huang and D. Ye, *Catal. Today*, 2013, 216, 220–228.
- 45 S. Afzal, X. Quan and J. Zhang, *Appl. Catal.*, B, 2017, 206, 692–703.
- 46 J. Wang, J. Li, C. Jiang, P. Zhou, P. Zhang and J. Yu, *Appl. Catal.*, B, 2017, 204, 147–155.
- 47 J. Zhu, H. Li, L. Zhong, P. Xiao, X. Xu, X. Yang, Z. Zhao and J. Li, *ACS Catal.*, 2014, 4, 2917–2940.
- 48 Y. Yu, J. Miao, J. Wang, C. He and J. Chen, *Catal. Sci. Technol.*, 2017, 7, 1590–1601.
- 49 D. Meng, Q. Xu, Y. Jiao, Y. Guo, Y. Guo, L. Wang, G. Lu and W. Zhan, *Appl. Catal.*, B, 2018, 221, 652–663.
- 50 M. H. Castaño, R. Molina and S. Moreno, *Appl. Catal.*, A, 2015, 492, 48–59.
- 51 P. Nakhostin Panahi, *Environ. Prog. Sustain. Energy*, 2017, 36, 1049–1055.
- 52 R. Zafari, M. Abdouss, Y. Zamani and A. Tavasoli, *Catal. Lett.*, 2017, 147, 2475–2486.

- 53 H. Huang, Y. Gu, J. Zhao and X. Wang, *J. Catal.*, 2015, 326, 54–68.
- 54 S. Royer, F. Bérubé and S. Kaliaguine, *Appl. Catal., A*, 2005, 282, 273–284.
- 55 S. Cao, H. Wang, F. Yu, M. Shi, S. Chen, X. Weng, Y. Liu and Z. Wu, *J. Colloid Interface Sci.*, 2016, 463, 233–241.
- 56 H. Huang, C. Zhang, L. Wang, G. Li, L. Song, G. Li, S. Tang and X. Li, *Catal. Sci. Technol.*, 2016, 6, 4260–4270.
- 57 M. Rahmani and M. Taghizadeh, *React. Kinet., Mech. Catal.*, 2017, 122, 409–432.
- 58 H. Wang, W. Yang, P. Tian, J. Zhou, R. Tang and S. Wu, *Appl. Catal., A*, 2017, 529, 60–67.